

A COMPARATIVE STUDY OF OPTICAL AND ULTRAVIOLET EFFECTIVE TEMPERATURES FOR DA WHITE DWARFS FROM THE *IUE* ARCHIVE

C.-P. Lajoie

*Department of Physics and Astronomy, McMaster University, Hamilton, Ontario, Canada,
L8S 4M1*

P. Bergeron

*Département de Physique, Université de Montréal, C.P. 6128, Succ. Centre-Ville,
Montréal, Québec, Canada, H3C 3J7.*

lajoiec@physics.mcmaster.ca, bergeron@astro.umontreal.ca

ABSTRACT

We present a comparative study of effective temperatures determined from the hydrogen Balmer lines and from the UV energy distribution for 140 DA white dwarfs drawn from the *IUE* archive. Our results indicate that the optical and UV temperatures of the majority of stars below $T_{\text{eff}} \sim 40,000$ K and within ~ 75 pc are in fairly good agreement given the uncertainties. At higher temperatures and/or larger distances, however, significant discrepancies are observed. Several mechanisms are investigated to account for these discrepancies including the effect of interstellar reddening, the presence of metals in the photosphere, and the existence of unresolved binary white dwarfs. The results of our analysis reveal that wavelength-dependent extinction is the most natural explanation for the observed temperature differences. We also attempt to predict the differences in optical and UV temperatures expected from unresolved degenerate binaries by performing an exhaustive simulation of composite model spectra. In light of these simulations, we then discuss some known double degenerates and identify new binary candidates by restricting our analysis to stars located within 75 pc where the effect of interstellar reddening is significantly reduced.

Subject headings: binaries: close – ISM: extinction – stars: atmosphere – stars: fundamental parameters – white dwarfs

1. INTRODUCTION

White dwarf stars are known to exist in two varieties: DA and non-DA stars. This spectral classification is primarily based on the presence (DA) or absence (non-DA) of hydrogen lines in their optical spectra. More precisely, non-DA stars have atmospheres mostly composed of helium but sometimes show weak hydrogen lines and prominent lines of heavier elements in the optical (see, e.g., Wesemael et al. 1993). The optical spectra of DA stars, on the other hand, are completely dominated by broad hydrogen absorption lines, while the ultraviolet (UV) part of their spectrum may also reveal the presence of weak metallic lines, although these lines tend to appear only at high effective temperatures ($T_{\text{eff}} \gtrsim 40,000$ K). From a theoretical point of view, the hydrogen atom is now fairly well understood, and the atmospheres of DA stars can be modeled to a high level of complexity. Fundamental parameters such as effective temperature and surface gravity can therefore be derived quite accurately for large samples of DA stars over a wide range of atmospheric parameters. The mass of these stars can also be obtained from detailed evolutionary models (e.g., Wood 1995). For instance, early pioneering work by Bergeron et al. (1992), and more recently by Liebert et al. (2005, hereafter LBH05), have used such model atmospheres to derive fundamental parameters of large samples of DA stars using this so-called spectroscopic method. Spectral analyses of different parts of the spectrum, however, and in particular a comparison of the atmospheric parameters obtained from other spectral regions could in principle help reveal interesting objects and/or possible caveats in the modeling of DA star atmospheres.

With the advent of UV astronomy, and in particular with the launch of the *International Ultraviolet Explorer (IUE)* space telescope in 1978, studies of this part of the spectrum have become possible. During its eighteen-year mission, *IUE* observed more than 320 degenerate stars at both low or high resolutions. Although the *IUE* spectral coverage does not fully include the Ly α line, the slope of the ~ 2000 Å wide energy distribution can be used successfully to measure the effective temperature. This new spectral window thus offers an excellent opportunity to verify the internal consistency of fundamental parameters obtained from different parts of the energy distribution. Unfortunately, only a few such studies exist in the literature. For instance, Barstow et al. (2001, 2003a) relied on *FUSE* data to estimate T_{eff} from the Lyman series, and they found significant discrepancies when compared with temperatures obtained from the Balmer line profiles in DA stars hotter than $T_{\text{eff}} \sim 50,000$ K. Although most DA stars with $T_{\text{eff}} \gtrsim 50,000$ K are now known to contain small traces of metals in their atmosphere, the authors attributed the observed discrepancies to deficiencies in the detailed physics incorporated in the model atmosphere calculations. The effect of metals on the determination of effective temperatures using the UV part of the spectrum has not been studied systematically, but some authors (Lanz & Hubeny 1995; Barstow et al. 2003a) have suggested that it might lead to an overestimate of T_{eff} when compared to the

optical determinations.

Assuming that the model atmospheres are accurate enough, discrepancies in the determination of the atmospheric parameters using different parts of the energy distribution might also reveal the presence of unresolved double degenerate (DD) binaries. This is appealing because binary white dwarfs are thought to be responsible for type Ia supernova explosions (SN Ia). In this scenario, two massive white dwarfs merge, resulting in an object with a mass exceeding the Chandrasekhar limit of $\sim 1.4 M_{\odot}$. Carbon and oxygen burning in degenerate conditions is then believed to lead to a thermonuclear runaway that completely disrupts the star. The search for these DDs has become a hot topic of research over the last few years, although observations of the bulk of this population has remained elusive, mostly because of their small expected angular separations. Radial velocity searches (e.g., Saffer et al. 1998; Maxted & Marsh 1999; Maxted et al. 2000) have revealed the presence of a few DDs with total masses close to the Chandrasekhar mass limit, but the numbers are still too low. Furthermore, most of the few known DDs have periods too long for them to merge within a Hubble time. All in all, there simply seems to be too few of them to account for the observed rate of SN Ia (Robinson & Shafter 1987; Bragaglia et al. 1990; Foss et al. 1991; Saffer et al. 1998). But there is hope: large surveys such as the *ESO Supernova Ia Progenitor Survey* (Napiwotzki et al. 2001, SPY) are now actively looking for these DD systems and should yield interesting results in the near future.

With these ideas in mind, we conducted a comparative study of effective temperatures determined from optical and UV observations for DA stars drawn from the *IUE* archive with the goal of identifying objects showing significant discrepancies in their temperature estimates. We describe respectively in § 2 and § 3 the observational material and theoretical framework used in our analysis. The effective temperature and surface gravity estimates are then presented in § 4 and discussed in § 5 where we show that most hot DA stars in our sample show significant discrepancies in their effective temperature determinations. Several possible sources of contamination are investigated, including interstellar reddening, the presence of heavy elements in the photospheric regions, and binarity. On the basis of our results, we then discuss in § 6 several interesting objects, including double degenerate candidates. Our conclusions follow in § 7.

2. OBSERVATIONS

Our main goal was to obtain the optical counterpart of all the DA stars observed by *IUE* during its 18-year mission. The *IUE* low-dispersion spectra used in this study come from the new reduction procedure of Holberg et al. (2003, hereafter HBB03), which follows

the prescription of Massa & Fitzpatrick (2000) for the correction of residual temporal and thermal effects, as well as absolute flux calibration. In fact, it is because this procedure is optimized for low-dispersion spectra of hot continuum sources that HBB03 have applied it to the complete sample of white dwarf stars observed by *IUE*. Given these corrections, along with the coaddition of multiple observations of the same object, this new reduction allows a significant gain in the signal-to-noise ratio (3% of the signal for optimally exposed spectra). The spectral coverage for the *IUE* spectra is about $\lambda\lambda 1150\text{--}1970$ (SWR camera) and $\lambda\lambda 1850\text{--}3150$ (LWR camera) at a resolution of ~ 6 Å and ~ 0.2 Å for the low- and high-dispersion modes, respectively. When combined, these two data sets cover a spectral range of about 2000 Å. Note that for some stars, only one of the two spectral regions is available. For more details on the cameras and the different setups used by *IUE*, see HBB03.

Among the ~ 320 degenerates observed by *IUE*, more than half are non-DA stars such as DB, DO, DP, DQ, DZ, or DC stars. Among the remaining DA stars, several have a bad UV spectrum that cannot be used in our analysis (WD 0104–464, 0216+143, 0250–026, 0517+307, 0518–105, 0531–022, 0646–253, 1053–550, 1159+803, 1413+231, 2116+736, 2205+250, and 2237+819). In addition, the *IUE* spectrum of WD 0935–371, which is a DA+DQ binary system, is actually that of the DQ star. Also, WD 0252–055, 0308+096, 0353+284, 0429+176, 1347–129, 1550+130, and 2110+300, all classified DA stars in HBB03, are found in binary systems with a bright companion that dominates or contaminates substantially the optical flux. These white dwarfs have thus been eliminated from our sample.

The optical spectra for the remaining DA stars have been obtained over several observing runs using the Steward Observatory 2.3 m telescope equipped with the Boller & Chivens spectrograph. The spectral coverage is about $\lambda\lambda 3100\text{--}5300$, thus covering $H\beta$ to $H9$ at an intermediate resolution of ~ 6 Å (FWHM). Objects south of declination ~ -30 degrees were excluded from our sample, although a few spectra in the Southern hemisphere were available from the analysis of Bragaglia et al. (1995) or provided by C. Moran (1999, private communication); these have a spectral resolution ranging from 3 to 9 Å (FWHM). Among the DA stars selected in our original sample, WD 0109–264, 1121+145, 1544+009, and 2333–002 turned out to be subdwarf stars, while WD 1055–072, previously classified DA7 in McCook & Sion (1999), is actually a featureless DC star. WD 0945+245 (DA+DX), 1015+014, and 1031+234 are magnetic white dwarfs, which cannot be easily analyzed within our theoretical framework, while WD 0950+139 shows strong emission lines produced by the faint planetary nebula. Also, WD 2246+066 (HS 2246+0640) is too hot ($T_{\text{eff}} \sim 140,000$ K according to our own estimate) and the Balmer lines are too weak to be analyzed with sufficient accuracy in our study. Finally, WD 1735–318 was too faint ($V = 18.1$) to be observed at Steward, while no references could be found in McCook & Sion (1999) for WD 0511–230. All in all, we end up with a sample of 140 DA stars for which both optical and

UV spectra are available. The optical spectra of this sample are displayed in Figures 1 and 2 in order of decreasing effective temperature, as determined in the next section.

3. MODEL ATMOSPHERES AND FITTING TECHNIQUE

The model atmospheres used in this analysis are described at length in LBH05 and references therein. The DA stars drawn from the *IUE* archive cover a wide range of effective temperatures including hot stars where non-local thermodynamic equilibrium (NLTE) effects are important ($T_{\text{eff}} \gtrsim 40,000$ K), and cooler stars where energy transport by convection dominates over radiative transport ($T_{\text{eff}} \lesssim 15,000$ K). Our model grid allows for both NLTE effects as well as energy transport by convection following the $\text{ML2}/\alpha = 0.6$ prescription of the mixing-length theory (see Bergeron et al. 1995). The theoretical spectra are calculated within the occupation formalism of Hummer & Mihalas (1988), which provides a detailed treatment of the level populations in the presence of perturbations from neighboring particles, as well as a consistent description of bound-bound and bound-free opacities. Our pure hydrogen model grid covers a range of effective temperature between $T_{\text{eff}} = 1500$ and $140,000$ K by steps of 500 K for $T_{\text{eff}} < 20,000$ K, and by steps of 5000 K above, and a range of $\log g$ between 6.5 and 9.5 by steps of 0.5 dex, with additional models at $\log g = 7.75$ and 8.25 .

The atmospheric parameters, T_{eff} and $\log g$, are first determined from the optical spectra using the so-called spectroscopic method (see, e.g. Bergeron et al. 1992), which relies on a comparison between synthetic and observed normalized profiles of the hydrogen Balmer lines. LBH05 have recently improved upon this method by using pseudo-Gaussian profiles or theoretical spectra to better define the continuum of each line (see LBH05 for more details). Given the fact that these lines are very sensitive to both T_{eff} and $\log g$, the normalized profiles for $\text{H}\beta$ to $\text{H}8$ are compared to model spectra, convolved with the appropriate Gaussian instrumental profile, using the nonlinear least-squares method of Levenberg-Marquardt (Press et al. 1986). Note that this χ^2 -minimization procedure uses all Balmer lines simultaneously to determine the atmospheric parameters. For cases where the red portion of the spectrum is contaminated by an unresolved main-sequence companion, we neglect $\text{H}\beta$ (WD 1026+002 and 1314+293) and, if necessary, $\text{H}\gamma$ as well (WD 0131–163, 0824+288, 1631+781, and 1636+351). Because of some irregularities in the line wings, $\text{H}\beta$ has also been omitted in the fits of WD 0410+117, 1650+724, and 1749+717.

For the UV portion of the spectrum, we determine T_{eff} in two independent ways. The first one relies on the slope of the UV energy distribution, which, as shown for instance by Bergeron et al. (1995, Fig. 10), is not very sensitive to surface gravity. For any assumed value of $\log g$, it is always possible to adjust the effective temperature to yield an equally

good fit to the UV observations. To overcome this problem, we fix $\log g$ to the optical value and determine T_{eff} using the slope of the UV energy distribution. Our fitting technique relies again on the nonlinear least-squares method of Levenberg-Marquardt. Here, the observed fluxes f_ν are compared to model Eddington fluxes H_ν using the relation

$$f_\nu = 4\pi(R/D)^2 H_\nu(T_{\text{eff}}, \log g) \quad (1)$$

where only T_{eff} and the solid angle $\pi(R/D)^2$ are considered free parameters. R/D is the ratio of the radius of the star to its distance from Earth. Note that this method for determining T_{eff} is only sensitive to relative fluxes, and it is therefore not subject to any error in the absolute flux calibration. However, any effect that may alter the *shape* of the UV energy distribution (e.g., interstellar reddening) might affect our T_{eff} estimates significantly. We will discuss some of these effects in § 5.

We obtain a second independent estimate of T_{eff} by normalizing the UV spectra to the measured V magnitude of each star (see also Finley et al. 1990). To do so, we first convert V into a mean flux using the relation

$$V = -2.5 \log f_\lambda^V + C_V \quad (2)$$

where f_λ^V is the average flux in the V bandpass, and $C_V = -21.0607$ is the flux constant for photon counting devices obtained by Holberg & Bergeron (2006) using new spectroscopic observations for Vega. We then divide each point of the observed and synthetic spectra by their respective flux at V and use the same minimization technique as above to estimate T_{eff} . With this approach, V is in fact used as a reference point around which synthetic spectra can be rotated until the UV flux is matched. This method is thus extremely sensitive to the absolute flux calibration scale, as well as to the accuracy of the V measurements. If for any reason the absolute fluxes are underestimated (*IUE* had only a $3''$ -diameter circular aperture, which could result in 50% or less light transmission in some cases) or if the V magnitudes have large uncertainties, this V -normalization method could lead to fairly bad estimates of the effective temperature.

Examples of both methods — UV-slope and V -normalization — for determining T_{eff} from the UV energy distributions are illustrated in Figure 3. We thus end up with three different estimates of T_{eff} for most of the 140 DA stars in our sample (4 objects in our sample do not have V measurements). These are compared in the next section. Interesting objects such as the unresolved double degenerate systems WD 0101+048 (Maxted et al. 2000), 0135–052 (Saffer et al. 1988), and 1022+050 (Maxted & Marsh 1999) are included in our sample. Any

discrepancy between their T_{eff} estimates could help confirm their binary status and validate our comparative approach as an efficient way to identify double degenerates.

4. RESULTS

Effective temperatures derived from the optical spectrum (T_{opt}), the slope of the UV energy distribution (T_{UV}), and the V -normalization method (T_V) for each object in our sample are reported in Table 1, together with the V magnitude, the surface gravity obtained from the optical solution ($\log g$), the mass (in solar masses), and the photometric distance (D). The V magnitudes are taken from the online version of the Villanova White Dwarf Catalog¹ and references therein, with the exception of WD 0421+740, 1650+724, 1827+778, and 2207–303, for which no measurements were available. Masses and radii are determined from the evolutionary models of Wood (1995) with carbon-core compositions, helium layers of $q(\text{He}) \equiv M_{\text{He}}/M_{\star} = 10^{-2}$, and thick hydrogen layers of $q(\text{H}) = 10^{-4}$. Photometric distances are obtained from the distance modulus, which is given by the relation

$$V - M_V = 5 \log_{10} D - 5 \quad (3)$$

where D is the distance to the star in parsecs, and M_V is the absolute magnitude interpolated in the photometric tables of Holberg & Bergeron (2006)² at the values of T_{eff} and $\log g$ determined from the optical solution. When no V magnitude is available, the distance is estimated from the solid angle $\pi(R/D)^2$ obtained from the UV-slope method, assuming that the *IUE* absolute fluxes are accurate.

Uncertainties for the optical solution are 1.2% in T_{eff} and 0.038 dex in $\log g$ (see § 2.4 of LBH05 for details). Uncertainties in T_{UV} and T_V are typically much larger, and they are estimated in the following way. We first calculate a standard deviation σ_0 :

$$\sigma_0^2 = \frac{1}{N} \sum_{i=1}^N \left[f_{\text{obs}}(\lambda_i) - f_{\text{bf}}(\lambda_i) \right]^2 \quad (4)$$

where $f_{\text{obs}}(\lambda_i)$ and $f_{\text{bf}}(\lambda_i)$ correspond respectively to the observed and the best-fit model fluxes at a given wavelength λ_i , and N is the number of data points in the UV spectrum. We

¹<http://www.astronomy.villanova.edu/WDCatalog/index.html>

²see <http://www.astro.umontreal.ca/~bergeron/CoolingModels/>

then change the effective temperature until the standard deviation between the corresponding model spectrum and our best-fit model equals σ_0 , providing us with a rough estimate of the 1σ uncertainty. Typically, errors in T_{UV} are much larger than errors in T_V because of the small sensitivity of the UV slope at high effective temperatures. For instance, the effective temperature uncertainty of a star near $T_{\text{eff}} \sim 50,000$ K, can be as large as the measurement itself, depending on the S/N ratio. On the other hand, the normalization at V provides much better leverage, and small variations of T_{eff} rapidly decrease the quality of the fit. The corresponding uncertainties are thus much smaller than with the UV-slope method. However, the V -normalization method is also very sensitive to the absolute *IUE* flux calibration, which is difficult to estimate. Uncertainties with both methods are reported in Table 1.

Figure 4 shows the mass distribution of all DA stars in our sample as a function of the optical effective temperature (T_{opt}). Objects are distributed fairly uniformly in effective temperature from ~ 7000 K ($\log T_{\text{eff}} = 3.85$ for WD 0135–052) up to $\sim 98,000$ K ($\log T_{\text{eff}} = 5.0$ for WD 0615+655), and in stellar mass in a range below $M \lesssim 0.45 M_{\odot}$ (for stars labeled in Fig. 4) up to the most massive objects like WD 0136+251 ($M = 1.22 M_{\odot}$) and 0346–011 (GD 50, $M = 1.27 M_{\odot}$). The low-mass degenerates are quite interesting from the point of view of binary evolution since the main-sequence lifetime of their progenitor is estimated to be much longer than the age of the Galaxy. These low-mass stars are thus believed to be the result of binary evolution. We address the question of how the existence of unresolved degenerate binaries may affect our temperature estimates in § 5.4.

The mass distribution of our sample is compared in Figure 5 to that obtained by LBH05 for the DA stars in the Palomar-Green (PG) Survey. Only stars with $T_{\text{eff}} > 13,000$ K are considered here since at lower temperatures, small amounts of helium are suspected to be brought to the surface by the hydrogen convection zone, thus increasing the atmospheric pressure and the inferred spectroscopic masses (Bergeron et al. 1990). It is comforting to see that both mass distributions compare favorably well despite the fact that the *IUE* archive does not constitute in any manner a complete statistical sample in magnitude or volume. We note in Figure 5, however, a clear deficiency of low-mass stars in our sample ($M < 0.45 M_{\odot}$) with respect to the PG sample. These have larger radii and should have been easily detected by *IUE* since they are more luminous than their high-mass counterparts. This bias against the presence of low-mass stars in our sample thus seems purely coincidental.

Finally, and most interestingly, all known ZZ Ceti stars included in our sample (WD 0133–116, 0858+363, 0921+354, 1116+026, 1236–495, 1307+354, 1425–811, 1559+369, 1647+591, 1855+338, 1935+276, and 2326+049) fall within the instability strip as defined by Gianninas et al. (2005, 2006), given the uncertainties in T_{UV} and T_V . No other objects are found within these limits, except for WD 1022+050 (LP 550-52), which is a known double

degenerate (Maxted & Marsh 1999).

5. DISCUSSION

5.1. Comparison of Optical and UV Temperatures

The effective temperatures obtained from optical spectroscopy (T_{opt} in Table 1) are compared with those obtained from the UV energy distribution in Figure 6 as a function of T_{opt} and in Figure 7 as a function of distance. The UV-slope (T_{UV} in Table 1) and V -normalization (T_V in Table 1) methods are shown in the upper and bottom panels, respectively. Instead of showing individual error bars in these plots, we use open circles to indicate the stars for which optical and UV effective temperatures are inconsistent (a few indicative errors bars are also displayed in Fig. 6). Here, we adopt a conservative criterion and assume that both estimates are inconsistent if the (absolute) difference in temperature is larger than 1.6σ (a 90% confidence level), where $\sigma^2 = \sigma^2(T_{\text{opt}}) + \sigma^2(T_V \text{ or } T_{\text{UV}})$.

Figure 6 shows that for stars below $\sim 40,000$ K, the optical and UV temperatures are in fairly good agreement ($\Delta T_{\text{eff}}/T_{\text{opt}} \lesssim 10\%$), while discrepancies up to 50% are observed for stars hotter than $\sim 40,000$ K. In the case of the UV-slope method, most of these large temperature differences are still consistent within the uncertainties (filled circles) because of the large errors associated with this method at high temperatures. In this case, only a few objects have statistically significant temperature differences. On the other hand, most of the large temperature differences observed with the V -normalization method are statistically inconsistent within uncertainties, suggesting that these differences are real and that some systematic effects may affect the temperature scale of hot DA stars.

Figure 7 also reveals a tendency for larger discrepancies with increasing distance. Furthermore, stars located within ~ 75 pc typically show a much better agreement between their three temperature estimates, even though a few nearby ($D \lesssim 75$ pc) objects still exhibit significant temperature differences. This suggests, once again, that some systematic effects may affect the temperature scale of more distant stars and, to a lesser extent, some nearby stars. Given the fact that hotter stars — which are often the most distant ones, as can be judged from the results of Table 1 — and distant stars show the most significant effective temperature discrepancies, we first study the possibility that interstellar reddening might be responsible for the trends shown in Figures 6 and 7.

5.2. Interstellar Reddening

Selective extinction from interstellar gas and dust can alter the shape of the UV energy distribution since it is more effective at short wavelengths (shortward of optical wavelengths). Following the prescription of Seaton (1979), we have simulated the effects of interstellar reddening on our optical and effective temperature determinations. To do so, we first apply to a model spectrum at a given effective temperature and surface gravity a wavelength-dependent extinction with an assumed color excess $E(B - V)$. We then fit this reddened spectrum with our standard unreddened model grid. We have run this simulation for synthetic spectra at various effective temperatures at $\log g = 8$ and with different color excesses. The predictions for both the UV-slope and V -normalization methods are displayed in Figure 8 together with the results for our DA sample. From these simulations, we see that interstellar reddening can easily reproduce the overall differences in measured effective temperatures, in the sense that a large color excess yields a large temperature difference, and this effect is more pronounced at high effective temperatures, a trend also observed in our sample. This is not an unexpected result, of course, since the UV part of the spectrum is more affected by reddening than the optical regions, and the flattening of the energy distribution results in an underestimation of the UV effective temperatures. The results shown in Figure 8 also reveal that the V -normalization method is much more sensitive to reddening than the UV-slope method. For instance, at $T_{\text{eff}} = 70,000$ K, the UV-slope method requires a color excess of $E(B - V) \sim 0.08$ in order to produce a $\sim 30\%$ difference in temperatures, while the V -normalization method requires a value of only $E(B - V) \sim 0.03$ to yield the same result. This is once again due to the fact that the V -normalization method is much more sensitive to small changes in the absolute UV fluxes.

To further validate our hypothesis, we must demonstrate that the color excesses required to account for the observed temperature discrepancies are not totally unrealistic, and that they agree reasonably well with observed values. We estimate these values for several DA stars in our sample by using the relation of Spitzer (1978, Fig. 1) between the hydrogen column densities and the $E(B - V)$ color excess

$$N(\text{H}) \approx 5.9 \times 10^{21} E(B - V) \quad [\text{mag}^{-1} \text{ cm}^{-2}] \quad (5)$$

combined with measurements of the column density taken from the literature (see Wolff et al. 1996, Marsh et al. 1997, Wolff et al. 1998, 1999, Bannister et al. 2003, and Good et al. 2004). The above relation includes the contribution of H I , H II , and H_2 and is consistent with X-ray and 21-cm observations towards globular clusters. As an example, we show by open circles in Figure 8 several objects in our sample that have been corrected for the effect

of reddening following the method described above. We see that in most cases, column densities taken from the literature lead to a much better agreement between temperature estimates. However, these same values of $E(B - V)$ do not agree well with those inferred from the theoretical curves of the UV-slope method. This is mostly because of the large uncertainties inherent to this particular method, and the location of the stars with respect to the reddening curves is to be interpreted with caution in this case. On the other hand, the values of $E(B - V)$ suggested by our theoretical simulations with the V-normalization method are fairly well corroborated by most of the measured values of $E(B - V)$. Moreover, the agreement in effective temperatures is also largely improved. This strongly suggests that reddening plays an important role in explaining the observed discrepancies in our effective temperature estimates, at least for distant stars.

5.3. Presence of Metals in Hot DA Stars

In this section, we investigate the effects produced by the presence of metals in the atmosphere of hot DA white dwarfs on the optical and UV energy distributions. Heavy elements have already been identified in the spectrum of most DA stars hotter than $\sim 40,000$ K from UV and extreme-UV observations (see, e.g., Vennes et al. 2006, and references therein). G191-B2B (WD 0501+527) is probably the most observed such metallic DA star and ions such as He, C, N, O, Si, S, P, Fe, and Ni have already been identified in its spectrum. Since metals block most of the flux at short wavelengths, the stellar flux is redistributed at longer wavelengths, and their presence in the atmospheres of hot DA stars could potentially affect the temperature structures and energy distributions. Because the observed metal abundances are significantly reduced in DA stars below $\sim 40,000$ K, radiative pressure has been naturally invoked as the mechanism responsible for maintaining these heavy elements in the atmospheric layers of hot white dwarf stars. This is precisely the effective temperature above which we observe the largest temperature discrepancies in Figures 6 and 7.

To study this effect, we start from a metal-rich synthetic spectrum, kindly provided to us by I. Hubeny (2005, private communication), and which is representative of G191-B2B at $T_{\text{eff}} = 54,000$ K, $\log g = 7.5$, with the metal abundances given in Barstow et al. (2003b). This spectrum is compared in Figure 9 with that of a pure hydrogen spectrum interpolated in our model grid for the same values of the atmospheric parameters. Note that both spectra have been calculated in a consistent manner using TLUSTY. From this comparison, we can see that indeed, the presence of metals has increased significantly the flux in the UV portion of the spectrum. We now fit the optical and UV fluxes of this metal-rich spectrum in the same manner as described in § 3 using our pure hydrogen model grid. The effective temperature

obtained from the Balmer line profiles is about 3000 K hotter than the true temperature of the model ($T_{\text{eff}} = 54,000$ K), while both T_{UV} and T_V are about ~ 6500 K hotter. Thus, the difference between UV and optical temperatures expected in metal-rich DA stars is *positive* when analyzed with pure hydrogen models, that is, above the dotted lines in Figures 6 and 7. In other words, had we fitted the DA stars in our sample with a grid of model atmospheres that include metals, we would have found even larger temperature discrepancies than those already observed here. This conclusion is similar to that reached by Lanz & Hubeny (1995) and Barstow et al. (1998, 2001, 2003a), who found that T_{eff} is overestimated in both optical and UV analyses when metals are present in the atmosphere of hot DA stars. We are thus forced to conclude that the temperature discrepancies observed in Figures 6 and 7 cannot be easily explained by the presence of metals in the hottest DA stars, or alternatively, by our use of pure hydrogen model atmospheres.

5.4. Unresolved Double Degenerates

As discussed in the Introduction, one the goals of this project was to search for unresolved double degenerate binaries by comparing effective temperatures determined from optical and ultraviolet spectra. As demonstrated by Liebert et al. (1991), it is impossible to infer the presence of such binary systems using the optical spectroscopic technique alone. Indeed, the coaddition of synthetic spectra of two DA stars with different values of T_{eff} and $\log g$ can be reproduced almost perfectly by a single DA spectrum. Hence, double degenerates would go totally unnoticed in an optical spectroscopic survey.

In this section, we extend the experiment of Liebert et al. (1991) by including the information contained in the UV energy distribution. Hence, we coadd the monochromatic fluxes of two synthetic spectra with random values of effective temperatures and surface gravities, properly weighted by their respective radius; because of the mass-radius relation, low-mass white dwarfs contribute more to the total flux than their more massive counterparts at the same temperature. We then fit these composite spectra and determine optical and UV temperatures in the same manner as described in § 3. Since in the minimization procedure there are always a cool and a hot solution on each side of the maximum strength reached by the Balmer lines, we always choose the solution with the lowest χ^2 value calculated from the difference between the simulated and best fit model spectra normalized at 4600 Å. When both fits are acceptable, which occurs when the temperatures of the two components are comparable, we retain both solutions. The results of our simulations up to $T_{\text{eff}} = 50,000$ K are displayed in Figure 10 for the UV-slope and V-normalization methods. At higher temperatures, the hot component of the system always dominates the total flux

and the predicted differences in optical and UV temperatures are too small to be measured efficiently with this technique.

Our results reveal that many fitted composite spectra show a good agreement between their three T_{eff} estimates. These binary systems correspond to those for which the total flux is almost completely dominated by the brightest component of the system, or to binaries that have very similar atmospheric parameters. These double degenerates would therefore go undetected with our comparative approach. Second, the results of Figure 10 indicate that most DA stars in our sample with temperature discrepancies larger than $\sim 20\%$ cannot be interpreted in terms of binarity alone, whatever method is used. Given the uncertainties in our T_{eff} determinations, double degenerates that could be detected by a comparison of optical and UV temperatures would rather be found at effective temperatures below $T_{\text{eff}} \sim 25,000$ K, or in regions where UV temperatures largely exceed the optical temperatures with the UV-slope method.

6. OBJECTS OF PARTICULAR INTEREST

Given the established dominant role of interstellar reddening in explaining the observed temperature differences, we now concentrate on nearby objects that are not significantly affected by reddening. The Sun is located in a region of the Galaxy where almost no dust and gas are found. The dimension of this Local Bubble ranges from 65 to 150 pc depending on the line of sight (Lallement et al. 2003). Beyond this, a wall of cold gas and dust with a typical HI column density of $\sim 3 \times 10^{19} \text{ cm}^2$ is observed. Thus, in order to minimize the effect of interstellar reddening, we restrict our analysis to objects located within 75 pc. Our results are presented in Figure 11 for both the UV-slope and V -normalization methods. Open symbols once again represent objects for which the temperatures are inconsistent within the uncertainties. These particular objects are labeled by their WD number in the figure and they are further discussed below along with other interesting objects.

WD 0101+048 (G2-17), 0135–052 (L870-2) — WD 0101+048 is a known binary star showing radial velocity variations (Maxted et al. 2000). However, the orbital period is uncertain: 1.2 or 6.4 days. Furthermore, the spectroscopic mass of $0.77 M_{\odot}$ is inconsistent with the photometric mass of $0.37 M_{\odot}$ obtained by Bergeron et al. (2001) based on its trigonometric parallax measurement. This discrepancy is likely due to the over-luminosity of the binary system (compared to a single star): an over-luminous object is then interpreted as a large-radius, less massive white dwarf. The location of WD 0101+048 in both panels of Figure 10 cannot be easily accounted for by our DD simulations, however. Furthermore, the optical and UV temperatures are consistent with both the UV-slope and V -normalization

methods. A similar conclusion can be reached for WD 0135–052, another known double degenerate system (Saffer et al. 1988), although in this case the temperature obtained from the UV-slope method is inconsistent with the optical value (Fig. 11). The measured temperature differences for these two stars are actually in the opposite sense from what is predicted by our simulations. We believe that the problem may be related to the inaccurate treatment of the UV opacity in our model atmosphere calculations at low temperatures. In particular, Kowalski & Saumon (2006) have shown that the red wing of the Ly α line of hydrogen can become an important opacity source in the UV when perturbations of hydrogen atoms by their interaction with molecular hydrogen are properly taken into account. This opacity source is not included in our model calculations and could affect our results.

WD 0346+011 (GD 50) — GD 50 is a massive DA star ($1.27 M_{\odot}$) showing unusual helium abundances (Vennes et al. 1996). Interestingly, one of most accepted formation scenarios for GD 50 is the merger of two white dwarfs (Bergeron et al. 1992; Segretain et al. 1997; García-Berro et al. 1997). The high mass and high effective temperature of this object suggest that GD 50 is relatively young, and a merger scenario would require this object to be in a relatively dense stellar environment. Dobbie et al. (2006) have argued on the basis of astrometric and spectroscopic data that GD 50 is actually a former member of the Pleiades cluster. Both methods for estimating the UV temperature yield similar values (Fig. 11 and Table 1). Only low column densities are measured in the line of sight of GD 50 so the difference of optical and UV temperatures cannot be explained in terms of reddening. Moreover, no radial velocity variations have ever been reported for this star. So given the particular nature of this object, it is difficult to draw any firm conclusion about its possible binary character.

WD 0348+339 (GD 52) — The difference in temperature observed in Figure 11 with the V-normalization method is only a 1.7σ result, and it is therefore not considered significant.

WD 0509–007 (RE J0512–004) — Even though all three T_{eff} estimates agree well for this object ($\sim 31,000$ K), its low mass of $0.40 M_{\odot}$ suggests a binary origin. Finley et al. (1997) have failed to see any flux excess up to 7500 \AA , suggesting that only a very cool companion or a similar white dwarf could be present. Our simulations with both methods also reproduce the location of this object in Figure 10, even though no radial velocity variations have been detected by Maxted et al. (2000). This object thus requires further investigation.

WD 0943+441 (G116-52) — This is a very interesting object. First, both estimates of the ultraviolet temperature differ by more than 5% from the optical value (see Fig. 11). Second, its location in Figure 10 can be easily reproduced by our simulations of unresolved binaries, suggesting that such temperature discrepancies could be the result of a composite spectrum. Finally, the low mass of WD 0943+441 ($0.39 M_{\odot}$) strongly supports a binary

evolution for this object. Unfortunately, no radial velocity measurements have been obtained for this star. We thus suggest that such measurements could reveal the binary nature of G116-52.

WD 1022+050 (LP 550-52) — This is another known double degenerate with measured radial velocity variations (Maxted & Marsh 1999). This star shows a temperature difference that exceeds $\sim 10\%$ with both methods used in our analysis (see Fig. 11). Our simulations displayed in Figure 10 are able to reproduce the observed temperature differences for this star quite nicely, indicating that the UV and optical energy distributions are altered by the presence of two stars in the system. We thus confirm with our approach the binary nature of WD 1022+050.

WD 1026+002 (PG) — This is a known binary consisting of a DA star and a M-dwarf companion. Contrary to our optical spectrum, the spectrum of Saffer et al. (1993) clearly shows the important contribution of the companion beyond $\sim 4500 \text{ \AA}$, i.e. at wavelengths longer than those used here to determine T_{opt} and $\log g$. Thus, the V magnitude is most likely contaminated by the companion, and this could easily explain the difference in temperatures reported here.

WD 1031-114 (L825-14) — The difference between T_V and T_{opt} is a $\sim 2.3 \sigma$ result for this star. Furthermore, we can easily reproduce the measured temperature differences with our simulations (Fig. 10), and L825-14 thus represents a good double degenerate candidate, despite the fact that no radial velocity variations have been detected by Maxted et al. (2000).

WD 2111+498 (GD 394) — GD 394 is a hot DA star (39,000 K) that shows atmospheric abundance inhomogeneities and photometric variations in the extreme UV portion of the spectrum. From their UV spectrum, Dupuis et al. (2000) show that effective temperatures determined from the UV continuum and from the Lyman line profiles differ by $\sim 4000 \text{ K}$, and that these temperature differences are likely due to dark spots at the surface of the star. Given the facts that no radial velocity variations have been observed by Saffer et al. (1998) and that the line of sight is not significantly reddened, no further conclusions can be reached for this star.

7. CONCLUSION

In summary, we have gathered optical and UV spectra for 140 DA white dwarfs for which we derived surface gravities and three different effective temperature determinations. We then performed an internal consistency check of all the effective temperature estimates and found that the observed discrepancies were most likely due to interstellar reddening.

The presence of metals in the atmosphere of DA stars has also been ruled out as a possible source of discrepancy since its effect would have been in the opposite direction of what we observed. Simulations of composite spectra have also shown that most of our objects do not exhibit composite spectra, therefore ruling out any binary nature. In order to limit the effect of interstellar reddening, we then restricted our sample to stars located within 75 pc from the Sun, and which show statistically significant temperature differences. This allowed us to identify interesting objects with inconsistent optical and UV effective temperatures that deserve further investigation. In particular, the very low masses of WD 0509–007 ($0.40 M_{\odot}$) and WD 0943+441 ($0.39 M_{\odot}$) are almost certainly indicative of past binary interactions and precise radial velocity measurements should reveal the presence of a companion. WD 1031–114 is also considered a good candidate on the basis of its effective temperature differences and clearly deserves further investigation.

We thank I. Hubeny for providing us with his synthetic spectrum of G191-B2B, and A. Gianninas for a careful reading of our manuscript. We also wish to thank the director and staff of the Steward Observatory for the use of their facilities. This work was supported in part by the NSERC Canada and by the Fund FQRNT (Québec). P. Bergeron is a Cottrell Scholar of Research Corporation.

REFERENCES

- Bannister, N.P., Barstow, M.A., Holberg, J.B., & Bruhweiler, F.C. 2003, MNRAS, 341, 477
- Barstow, M.A., Good, S.A., Burleigh, M.R., Hubeny, I., Holberg, J.B., & Levan, A.J. 2003a, MNRAS, 344, 562
- Barstow, M.A., Good, S.A., Holberg, J.B., Hubeny, I., Bannister, N.P., Bruhweiler, F.C., Burleigh, M.R., & Napiwotzki, R. 2003b, MNRAS, 341, 870
- Barstow, M.A., Holberg, J.B., Hubeny, I., Good, S.A., Levan, A.J., & Meru, F. 2001, MNRAS, 328, 211
- Barstow, M.A., Hubeny, I., & Holberg, J.B. 1998, MNRAS, 299, 520
- Bergeron, P., Leggett, S.K., & Ruiz, M.T. 2001, ApJS, 133, 413
- Bergeron, P., Saffer, R.A., & Liebert, J. 1992, ApJ, 394, 228
- Bergeron, P., Wesemael, F., Fontaine, G., & Liebert, J. 1990, ApJ, 351, L21
- Bergeron, P., Wesemael, F., Lamontagne, R., Fontaine, G., Saffer, R.A., & Allard, N.F. 1995, ApJ, 449, 258
- Bragaglia, A., Greggio, L., Renzini, A., & D’Odorico, S. 1990, ApJ, 365, 13
- Bragaglia, A., Renzini, A., & Bergeron, P. 1995, ApJ, 443, 735
- Dobbie, P.D., Napiwotzki, R., Lodieu, N., Burleigh, M.R., Barstow, M.A., & Jameson, R.F. 2006, MNRAS, 373, L45
- Dupuis, J., Chayer, P., Vennes, S., Christian, D.J., & Kruk, J.W. 2000, ApJ, 537, 977
- Finley, D.S., Basri, G., & Bowyer, S. 1990, ApJ, 359, 483
- Finley, D.S., Koester, D., & Basri, G. 1997, ApJ, 488, 375
- Foss, D., Wade, R.A., & Green, R.F. 1991, ApJ, 374, 281
- García-Berro, E., Isern, J., & Hernanz, M. 1997, MNRAS, 289, 973
- Gianninas, A., Bergeron, P., & Fontaine, G. 2005, ApJ, 631, 1100
- Gianninas, A., Bergeron, P., & Fontaine, G. 2006, AJ, 132, 831

- Good, S.A., Barstow, M.A., Holberg, J.B., Sing, D.K., Burleigh, M.R., & Dobbie, P.D. 2004, MNRAS, 355, 1031
- Holberg, J.B., Barstow, M.A., & Burleigh, M.R. 2003, ApJS, 147, 145 (HBB03)
- Holberg, J.B., & Bergeron, P. 2006, AJ, 132, 1221
- Hummer, D.G., & Mihalas, D. 1988, ApJ, 331, 794
- Kowalski, P.M., & Saumon, D. 2006, ApJ, 651, L137
- Lallement, R., Welsh, B.Y., Vergely, J.L., Crifo, F., & Sfeir, D. 2003, A&A, 411, 447
- Lanz, T., & Hubeny, I. 1995, ApJ, 439, 905
- Liebert, J., Bergeron, P., & Holberg, J.B. 2005, ApJS, 156, 47 (LBH05)
- Liebert, J., Bergeron, P., & Saffer, R. A. 1991, in White Dwarfs, ed. G. Vauclair & E.M. Sion (Kluwer: Dordrecht), 409
- Marsh, M.C., Barstow, M.A., Buckley, D.A., Burleigh, M.R., Holberg, J.B., Koester, D., O'Donoghue, D., Penny, A.J., & Sansom, A.E. 1997, MNRAS, 287, 705
- Massa, D., & Fitzpatrick, E.L. 2000, ApJS, 126, 517
- Maxted, P.F.L., & Marsh, T.R. 1999, MNRAS, 307, 122
- Maxted, P.F.L., Marsh, T.R., & Moran, C.K.J. 2000, MNRAS, 319, 305
- McCook, G.P., & Sion, E.M. 1999, ApJS, 121, 1
- Napiwotzki, R., Edelmann, H., Heber, U., Karl, C., Drechsel, H., Pauli, E.-M., & Christlieb, N. 2001, A&A, 378, 17
- Press, W.H., Flannery, B.P., & Teukolsky, S.A. 1986, Numerical Recipes (Cambridge: Cambridge University Press)
- Robinson, E.L., & Shafter, A.W. 1987, ApJ, 322, 296
- Saffer, R.A., Liebert, J., & Olszewski, E.W. 1988, ApJ, 334, 947
- Saffer, R.A., Livio, M., & Yungelson, L.R. 1998, ApJ, 502, 394
- Saffer, R.A., Wade, R.A., Liebert, J., Green, R.F., Sion, E.M., Bechtold, J., Foss, D., & Kidder, K. 1993, AJ, 105, 1945

- Seaton, M.J. 1979, MNRAS, 187, 73
- Segretain, L., Chabrier, G., & Mochkovitch, R. 1997, ApJ, 481, 355
- Spitzer, L., Jr. 1978, Physical processes in the interstellar medium, 1st edn. (New York: John Wiley & Sons)
- Vennes, S., Bowyer, S., & Dupuis, J. 1996, ApJ, 461, 103
- Vennes, S., Chayer, P., Dupuis, J., & Lanz, T. 2006, ApJ, 652, 1554
- Wesemael, F., Greenstein, J.L., Liebert, J., Lamontagne, R., Fontaine, G., Bergeron, P. & Glaspey, J.W. 1993, PASP, 105, 761
- Wolff, B., Jordan, S., & Koester, D. 1996, A&A, 307, 149
- Wolff, B., Koester, D., Dreizler, S., & Haas, S. 1998, A&A, 329, 1045
- Wolff, B., Koester, D., & Lallement, R. 1999, A&A, 346, 969
- Wood, M.A. 1995, in 9th European Workshop on White Dwarfs, NATO ASI Series, ed. D. Koester & K. Werner (Berlin: Springer), 41

Table 1. Atmospheric Parameters for IUE DA White Dwarf Stars

WD	Name	V	T_{opt} (K)	$\log g$	T_{UV} (K)	T_V (K)	M/M_{\odot}	D (pc)
0004+330	GD 2	13.82	48385	7.68	42726 \pm 9600	42555 \pm 3900	0.55	109.5
0037+312	GD 8	14.66	49564	7.72	28452 \pm 5400	30474 \pm 3500	0.57	158.0
0047–524	BPM 16274	14.20	18339	7.83	18223 \pm 900	18559 \pm 350	0.53	51.8
0050–332	GD 659	13.36	34529	7.99	35077 \pm 4000	33936 \pm 2000	0.65	55.9
0101+048	G2-17	13.96	8530	8.27	7912 \pm 900	7903 \pm 450	0.77	14.3
0131–163	GD 984	13.98	44015	8.00	42553 \pm 8400	38905 \pm 3700	0.68	86.2
0133–116	Ross 548	14.16	11986	7.98	12054 \pm 800	11979 \pm 400	0.60	32.5
0134+833	GD 419	13.06	18311	8.06	18542 \pm 1000	18744 \pm 400	0.66	26.1
0135–052	L870-2	12.84	7273	7.85	6319 \pm 500	6747 \pm 450	0.51	8.6
0136+251	PG 0136+251	16.00	39791	9.03	38660 \pm 5000	39209 \pm 6200	1.22	85.4
0145–257	GD 1401	14.69	25625	7.97	25319 \pm 2600	21836 \pm 975	0.62	78.3
0148+467	GD 279	12.17	13432	7.93	13553 \pm 400	13213 \pm 200	0.57	14.7
0205+250	G35-29	13.23	20243	7.90	20449 \pm 2500	19334 \pm 600	0.57	34.2
0214+568	H Per 1166	13.65	21408	7.91	21338 \pm 1500	21990 \pm 500	0.58	43.1
0227+050	Feige 22	12.79	18887	7.84	18219 \pm 1250	18708 \pm 450	0.54	27.5
0229–481	LB 1628	14.53	71970	7.09	46972 \pm 17500	48200 \pm 8250	0.46	325.9
0231–054	GD 31	14.24	13552	8.66	12949 \pm 400	13152 \pm 200	1.02	22.7
0232+035	Feige 24	12.40	63698	7.25	51306 \pm 14500	41356 \pm 2250	0.47	97.7
0232+525	G174-5	13.75	16892	8.27	16211 \pm 1000	16633 \pm 425	0.79	29.0
0255–705	BPM 2819	14.08	10608	8.15	10564 \pm 2500	10251 \pm 1275	0.70	24.0
0302+027	Feige 31	14.97	35337	7.84	35916 \pm 10000	33620 \pm 2800	0.58	133.7
0310–688	LB 3303	11.40	15658	8.09	15487 \pm 600	15962 \pm 325	0.67	10.5
0320–539	LB 1663	14.99	34443	7.75	30966 \pm 3400	32745 \pm 2375	0.54	140.8
0343–007	KUV 03439–0048	14.91	62859	7.73	46058 \pm 12200	37759 \pm 4750	0.61	201.1
0346–011	GD 50	13.99	41196	9.15	36456 \pm 3800	36241 \pm 1550	1.27	30.8
0348+339	GD 52	15.20	14194	8.20	13391 \pm 600	13605 \pm 300	0.74	51.8
0352+096	HZ 4	14.34	14033	8.19	13964 \pm 600	13699 \pm 250	0.73	34.7
0401+250	G8-8	13.81	12240	7.99	12200 \pm 400	12291 \pm 250	0.60	28.0
0406+169	LB 227	15.13	15073	8.26	14650 \pm 600	14624 \pm 300	0.78	50.4
0410+117	HZ 2	13.86	20504	8.01	20134 \pm 1200	20251 \pm 400	0.63	43.0
0413–077	40 Eri B	9.52	16480	7.87	16093 \pm 600	16483 \pm 300	0.55	5.4
0421+740	RE J0427+741	—	52372	7.85	46006 \pm 16000	—	0.63	203.6
0425+168	GH 7-233	14.06	23760	8.08	23076 \pm 2200	23224 \pm 950	0.68	50.7
0453+418	GD 64	13.89	13564	7.74	13688 \pm 700	13684 \pm 400	0.47	37.1
0455–282	RE J0457–280	13.95	56087	7.90	58265 \pm 20000	52821 \pm 5450	0.66	104.9
0501+527	G191-B2B	11.78	58865	7.57	60680 \pm 15000	57414 \pm 4700	0.54	52.7
0507+045	HS 0507+0435A	14.30	20787	7.99	20587 \pm 2800	21147 \pm 700	0.62	53.7
0509–007	RE J0512–004	13.80	32004	7.37	30931 \pm 4000	30475 \pm 1575	0.40	102.2
0548+000	GD 257	14.77	45871	7.75	38384 \pm 8800	34631 \pm 3600	0.57	155.7
0549+158	GD 71	13.04	33212	7.85	31034 \pm 2200	31943 \pm 1000	0.58	51.5
0612+177	G104-27	13.39	25312	7.94	25132 \pm 1800	25817 \pm 675	0.61	43.4
0615+655	HS 0615+6535	15.70	97889	7.12	63424 \pm 39500	27217 \pm 4550	0.56	682.3
0621–376	RE J0623–374	12.09	59779	7.24	53791 \pm 20500	58154 \pm 11625	0.45	81.8
0631+107	WD 0631+107	13.82	26718	7.87	26291 \pm 2600	28803 \pm 1650	0.57	58.6
0644+375	G87-7	12.07	21300	8.16	21349 \pm 2400	21519 \pm 450	0.72	17.4

Table 1—Continued

WD	Name	V	T_{opt} (K)	$\log g$	T_{UV} (K)		T_V (K)		M/M_{\odot}	D (pc)
0651−020	GD 80	14.83	33643	8.23	32669	± 3400	32853	± 1775	0.79	89.8
0802+413	KUV 08026+4118	15.21	51616	7.59	33905	± 6400	37049	± 4400	0.53	231.5
0824+288	PG 0824+289	14.73	50525	7.75	40603	± 7000	36841	± 2275	0.58	161.5
0836+237	PG 0836+237	16.64	54290	7.71	48595	± 27500	39357	± 4825	0.58	415.8
0839−327	LHS 253	11.90	9318	7.99	9071	± 400	9238	± 300	0.59	8.0
0858+363	GD 99	14.76	11825	8.09	11790	± 650	11650	± 400	0.66	39.4
0904+511	PG 0904+512	16.40	32268	8.25	32111	± 9500	30669	± 2650	0.80	175.2
0921+354	G117-B15A	15.50	11627	7.98	12132	± 800	12028	± 350	0.59	58.5
0939+262	PG 0939+262	14.53	68201	7.84	47613	± 12400	38903	± 2950	0.66	159.3
0943+441	G116-52	13.29	12822	7.55	13868	± 1400	13807	± 550	0.39	30.0
0947+857	RE J0957+852	15.80	51709	8.02	36908	± 8000	39539	± 4125	0.71	214.5
0954−710	BPM 6082	13.48	13930	7.76	13894	± 600	14200	± 425	0.49	30.9
1010+064	PG 1010+065	16.61	45329	7.96	39478	± 17000	39885	± 7575	0.66	304.3
1022+050	LP 550-52	14.18	13828	7.47	11745	± 600	11645	± 450	0.36	51.1
1026+002	PG 1026+002	13.83	17172	7.97	16620	± 1100	16261	± 400	0.60	37.6
1026+453	PG 1026+454	16.13	35900	7.91	38734	± 12000	33748	± 3300	0.62	219.0
1031−114	L825-14	13.02	25328	7.89	23865	± 2200	23399	± 800	0.58	37.9
1033+464	GD 123	14.34	29425	7.88	28487	± 2600	27772	± 850	0.58	81.8
1041+580	PG 1041+580	14.60	30436	7.75	29363	± 4800	28813	± 1525	0.53	104.4
1042−690	BPM 6502	12.87	21012	7.93	21250	± 1800	20826	± 600	0.59	29.2
1052+273	GD 125	14.11	23095	8.37	22480	± 1200	23039	± 450	0.86	40.8
1056+516	LB 1919	16.76	67022	7.99	39045	± 18000	57701	± 18400	0.72	388.4
1057+719	PG 1057+719	14.80	41276	7.80	36555	± 6200	39394	± 3600	0.58	142.3
1104+602	WD 1104+602	13.80	17922	8.02	17815	± 1600	18070	± 575	0.63	37.3
1105−048	L970-30	12.92	15142	7.85	14936	± 600	14780	± 300	0.53	24.2
1108+325	PG 1108+325	16.80	62364	7.61	45281	± 21500	42007	± 6500	0.56	530.5
1109+244	PG 1109+244	15.77	37812	8.14	37047	± 10800	36305	± 4175	0.74	161.9
1116+026	PG 1116+026	14.57	12286	8.05	12198	± 300	12211	± 150	0.63	38.3
1123+189	PG 1123+189	14.13	51751	7.90	49004	± 12800	42837	± 3575	0.65	109.6
1134+300	GD 140	12.52	21259	8.55	21199	± 800	21447	± 400	0.97	16.0
1143+321	G148-7	13.66	15276	7.90	15016	± 650	15619	± 425	0.56	33.1
1234+481	HS 1234+4811	14.42	53843	7.72	51701	± 14200	49703	± 5700	0.58	148.0
1236−495	BPM 37093	13.96	11809	8.84	11656	± 650	11887	± 425	1.12	15.0
1254+223	GD 153	13.35	39615	7.86	36519	± 4200	36932	± 2100	0.60	67.9
1307+354	GD 154	15.31	11180	8.15	11473	± 800	11328	± 500	0.70	45.4
1314+293	HZ 43	12.98	52394	8.06	49785	± 10600	51931	± 3200	0.73	57.2
1327−083	Wolf 485	12.05	13823	7.80	13762	± 300	13570	± 150	0.50	15.5
1337+705	G238-44	12.78	20390	7.94	19954	± 1000	20298	± 300	0.59	27.3
1403−077	PG 1403−077	15.82	50664	7.62	37519	± 17000	48595	± 10300	0.54	296.7
1413+015	PG 1413+015	17.01	49716	7.68	41897	± 14500	31394	± 3350	0.55	483.1
1425−811	L19-2	13.35	12098	8.21	12244	± 350	12203	± 200	0.74	19.3
1532+033	PG 1532+033	16.02	66495	7.57	36114	± 8800	47257	± 7700	0.56	398.1
1544−377	L481-60	13.07	10583	8.09	10436	± 400	10259	± 275	0.66	15.7
1548+405	PG 1548+405	15.89	54476	7.64	44464	± 19500	45863	± 7200	0.56	313.7
1559+369	G180-23	14.36	11160	8.04	11235	± 750	11045	± 525	0.63	31.6

Table 1—Continued

WD	Name	V	T_{opt} (K)	$\log g$	T_{UV} (K)	T_V (K)	M/M_{\odot}	D (pc)
1615–154	G153-41	13.40	28971	7.95	29620 \pm 2800	29373 \pm 1125	0.62	49.5
1620–391	CD –38 10980	10.99	24231	8.07	24020 \pm 1000	23991 \pm 400	0.68	12.6
1631+781	WD 1631+781	13.28	41489	7.97	40496 \pm 7000	38293 \pm 2800	0.66	61.8
1636+351	KUV 16366+3506	15.02	36599	7.99	39212 \pm 10200	36590 \pm 4950	0.66	125.8
1647+591	G226-29	12.23	12460	8.29	12223 \pm 400	12272 \pm 150	0.79	11.2
1650+724	HS 1650+7229	—	44334	7.52	40820 \pm 25500	—	0.49	588.6
1657+343	PG 1657+344	16.42	52488	7.62	42918 \pm 19000	41088 \pm 6275	0.54	398.8
1713+695	G240-51	13.27	15241	7.86	14908 \pm 1500	15548 \pm 825	0.54	28.3
1725+586	PG 1725+587	15.70	56084	8.31	49639 \pm 24000	50541 \pm 7800	0.87	168.0
1738+669	RE J1737+665	14.60	81210	7.77	56962 \pm 20000	64926 \pm 13700	0.67	193.7
1749+717	HS 1749+7145	15.70	69363	7.53	36931 \pm 12000	34196 \pm 2750	0.56	365.3
1800+685	KUV 18004+6836	14.72	44176	7.82	47201 \pm 16000	42105 \pm 8600	0.60	140.5
1819+580	RE J1820+580	13.93	43634	7.93	45125 \pm 16000	44704 \pm 9500	0.64	88.9
1827+778	HS 1827+7753	—	74351	7.50	48129 \pm 22000	—	0.57	410.7
1828+668	KUV 18824+6650	16.65	10798	8.20	10936 \pm 4000	10216 \pm 1100	0.73	77.7
1845+019	Lanning 18	12.95	29384	7.81	28478 \pm 2800	28621 \pm 900	0.55	45.2
1845+683	KUV 18453+6819	15.50	37084	8.20	37563 \pm 10000	43338 \pm 5500	0.77	134.9
1855+338	G207-9	14.63	11958	8.36	11952 \pm 600	12055 \pm 400	0.83	30.9
1919+145	GD 219	12.98	14430	8.06	14521 \pm 800	14935 \pm 450	0.65	20.7
1935+276	G185-32	13.03	12123	8.06	12024 \pm 450	12039 \pm 275	0.64	18.6
1936+327	GD 222	13.58	21329	7.91	20679 \pm 2800	21153 \pm 700	0.58	41.8
1950–432	MCT 1950–4314	14.86	39424	7.86	34706 \pm 7000	31565 \pm 2125	0.60	135.1
1953–011	L997-21	13.69	7772	8.24	7150 \pm 1000	7637 \pm 625	0.75	11.0
2007–303	LTT 7987	12.18	14454	7.86	14660 \pm 800	14913 \pm 400	0.54	16.5
2014–575	L210-114	13.70	27465	7.94	26761 \pm 2200	26231 \pm 725	0.61	54.3
2020–425	MCT 2020–4234	14.90	29165	8.10	31689 \pm 10400	27170 \pm 1275	0.70	89.3
2028+390	GD 391	13.38	24127	7.90	24398 \pm 1600	24132 \pm 450	0.58	42.6
2032+248	Wolf 1346	11.52	19953	7.90	19936 \pm 1200	19991 \pm 450	0.57	15.4
2039–202	L711-10	12.33	19188	7.93	18575 \pm 1200	19169 \pm 400	0.58	21.2
2046+396	KPD 2046+3940	14.43	65428	7.51	50532 \pm 22000	50801 \pm 5800	0.54	200.9
2047+372	G210-36	12.93	14069	8.21	14064 \pm 600	14291 \pm 350	0.74	17.9
2105–820	BPM 1266	13.62	10794	8.19	10385 \pm 1300	10674 \pm 750	0.72	19.4
2111+498	GD 394	13.08	39205	7.81	32788 \pm 3800	34750 \pm 2575	0.58	61.6
2117+539	G231-40	12.26	13991	7.78	14002 \pm 1200	14360 \pm 550	0.49	17.5
2126+734	GW +73 8031	12.83	15287	7.84	15012 \pm 700	15393 \pm 400	0.53	23.5
2136+828	G261-45	13.02	16905	7.86	16782 \pm 800	17488 \pm 500	0.55	27.4
2146–433	MCT 2146–4320	15.81	63711	7.53	121884 \pm 96000	21596 \pm 1825	0.55	364.7
2149+021	G93-48	12.74	17360	7.93	16801 \pm 1000	17248 \pm 350	0.58	23.6
2153–419	MCT 2153–4156	15.38	40974	8.01	27792 \pm 13000	21549 \pm 2900	0.68	157.2
2159–414	MCT 2159–4129	15.88	61277	7.48	44506 \pm 18000	54528 \pm 11100	0.52	386.2
2207–303	RE J2210–300	—	28245	7.86	27871 \pm 3600	—	0.57	74.3
2246+223	G67-23	14.35	10647	8.80	10161 \pm 1000	10559 \pm 450	1.10	16.1
2309+105	GD 246	13.09	54681	7.94	51498 \pm 11800	50217 \pm 3100	0.68	67.3
2326+049	G29-38	13.06	11817	8.15	11632 \pm 400	11626 \pm 175	0.70	17.3
2331–475	MCT 2331–473	13.46	52574	7.78	50344 \pm 15200	48697 \pm 4500	0.60	89.1

Table 1—Continued

WD	Name	V	T_{opt} (K)	$\log g$	T_{UV} (K)	T_V (K)	M/M_{\odot}	D (pc)
2341+322	L1512-34B	12.90	12573	7.93	12339 \pm 350	12420 \pm 250	0.57	19.5
2349+286	PG 2349+286	16.26	37606	7.99	37906 \pm 17500	31465 \pm 6975	0.66	226.1
2353+026	PG 2353+026	15.83	60943	7.60	51961 \pm 25000	33591 \pm 3400	0.56	336.2
2357+296	PG 2357+297	15.10	52022	7.53	37553 \pm 7000	44920 \pm 5500	0.51	233.3
2359–434	L362-81	12.95	8544	8.44	7832 \pm 1000	8148 \pm 300	0.88	8.4

Fig. 1.— Optical spectra for our sample of DA stars selected from the *IUE* archive. The spectra are normalized at 4600 Å and are shifted vertically for clarity. The effective temperature decreases from upper left to bottom right.

Fig. 2.— Same as Fig. 1.

Fig. 3.— Sample fits to the UV energy distribution using the slope method (*blue*) and the *V*-normalization method (*red*) to determine T_{eff} . In both cases, we assume the $\log g$ value obtained from the optical spectrum.

Fig. 4.— Mass distribution for all the DA stars in our sample as a function of T_{opt} . The objects labeled in the figure correspond to low-mass stars ($M \lesssim 0.45 M_{\odot}$), which must have evolved in a binary system since the main-sequence lifetime of their progenitor is estimated to be longer than the age of the Galaxy.

Fig. 5.— Mass distribution for the DA stars in our sample hotter than 13,000 K compared to the mass distribution obtained by LBH05 for the DA stars in the PG survey in the same temperature range.

Fig. 6.— Differences in optical (T_{opt}) and ultraviolet ($T_{V/\text{UV}}$) effective temperatures (normalized to T_{opt}) as a function of T_{opt} . The UV-slope and *V*-normalization methods are used in the top and bottom panel, respectively. Open circles represent objects for which optical and UV temperature estimates are inconsistent within the uncertainties. A few indicative error bars are also shown, together with the average error bar in the lower left corner of each panel.

Fig. 7.— Same as Fig. 6 but as a function of distance.

Fig. 8.— Effect of interstellar reddening on the temperature differences as determined from the UV-slope (*top*) and *V*-normalization (*bottom*) methods. The color excess $E(B - V)$ for each simulation is indicated on the right side of each curve. Results for our DA sample are shown by filled circles, while objects corrected for reddening are represented by open circles and connected by dashed lines to the corresponding unreddened solutions.

Fig. 9.— Synthetic spectrum of a model at $T_{\text{eff}} = 54,000$ K and $\log g = 7.5$ that includes H, He, C, N, O, Si, Fe, and Ni (*solid line*) compared to a pure hydrogen synthetic spectrum with the same atmospheric parameters (*dotted line*). Both spectra have been normalized at 5500 Å and convolved with a 6 Å FWHM instrumental profile.

Fig. 10.— Simulated temperature differences for unresolved binary white dwarf systems using the UV-slope method (*top*) and the *V*-normalization method (*bottom*). Small red dots

correspond to our simulations while the results for our sample of DA stars are represented by circles. Filled circles with labels and error bars are discussed in § 6. [*See the electronic version of the Journal for a color version of this figure.*]

Fig. 11.— Differences in optical and UV temperatures for stars located within 75 pc. Both the UV-slope method (*circles*) and the *V*-normalization method (*triangles*) are shown here. Objects with inconsistent temperatures are shown with open symbols, labeled by their WD number, and discussed in § 6.

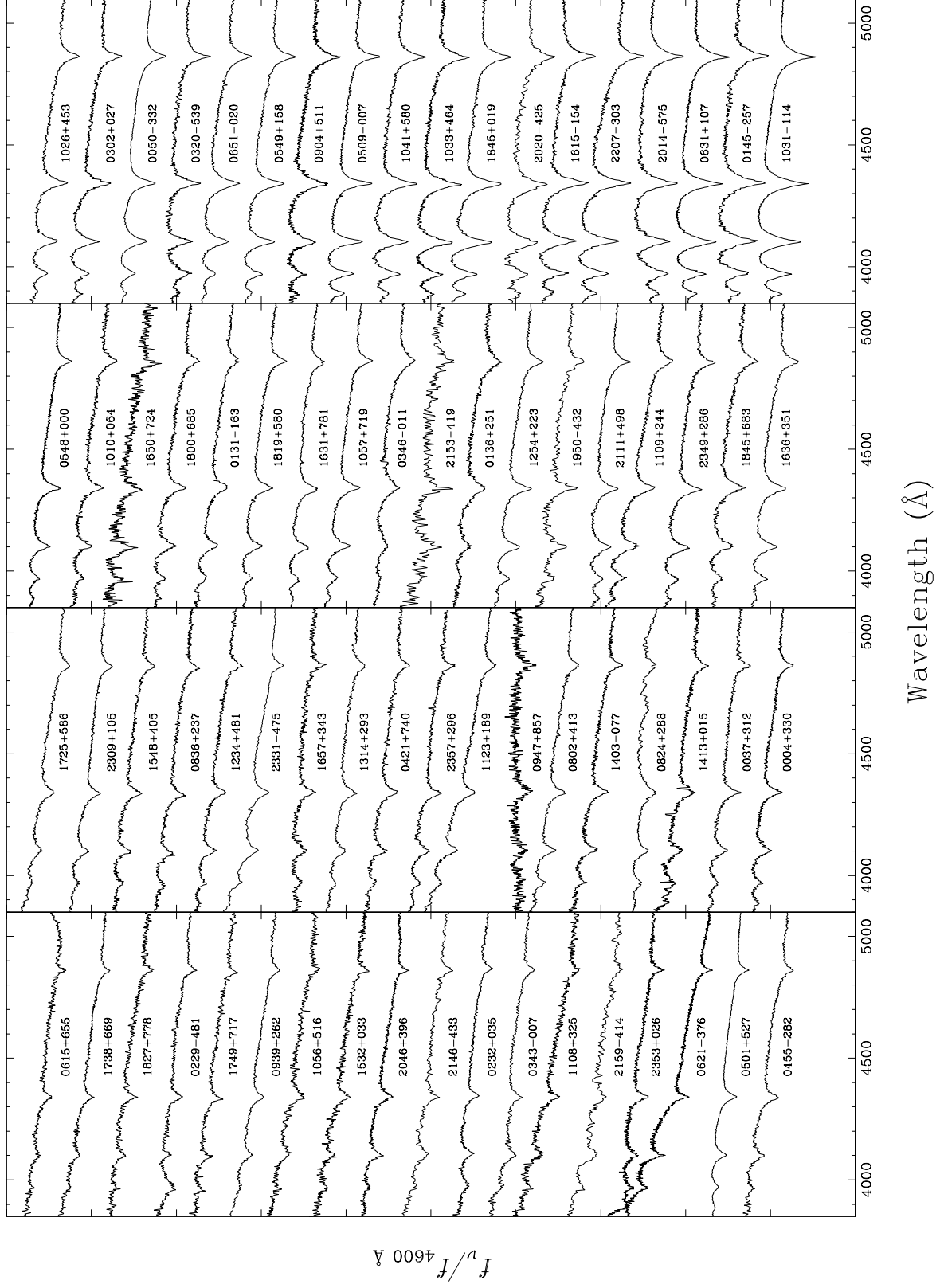


Figure 1

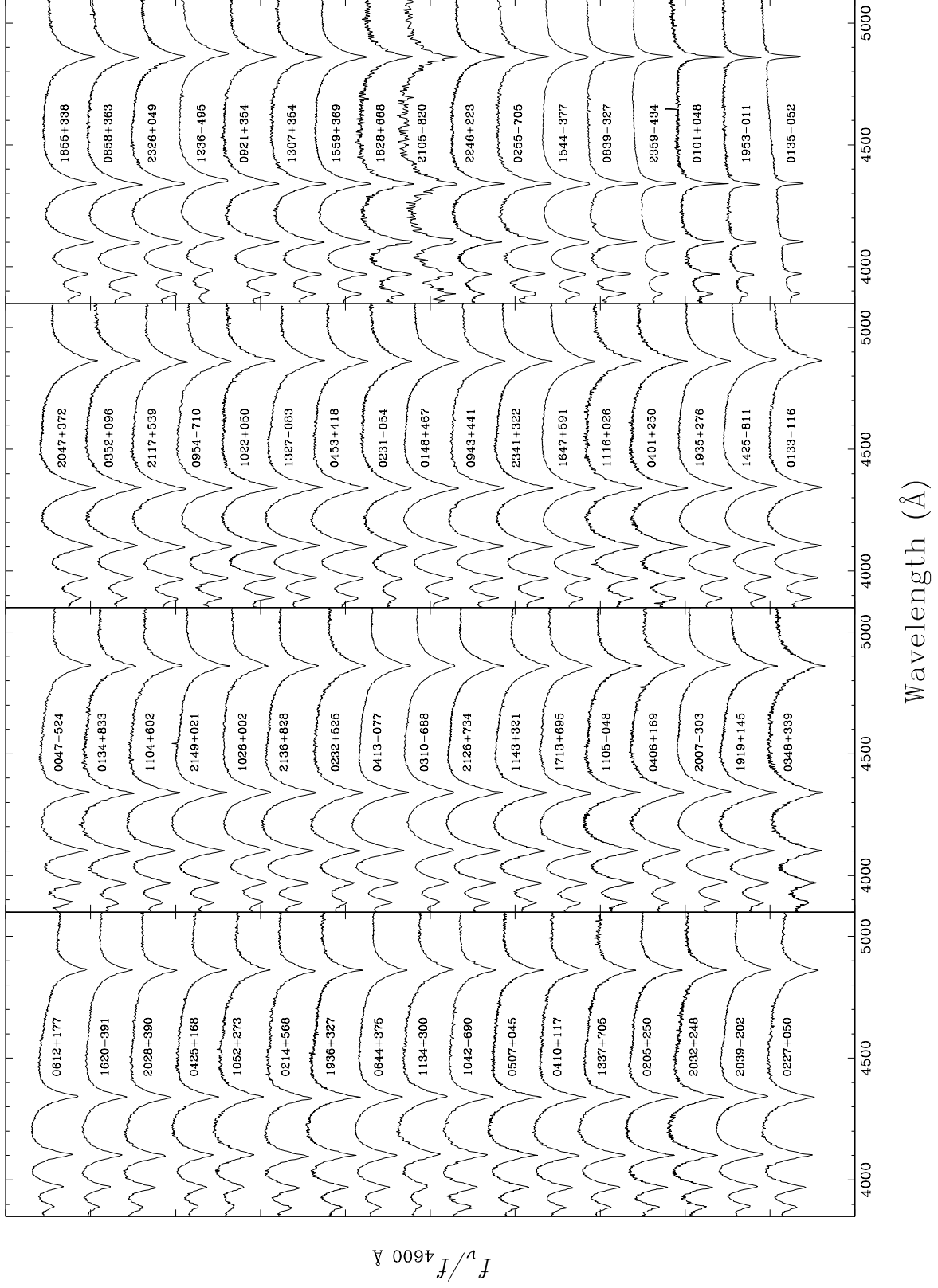


Figure 2

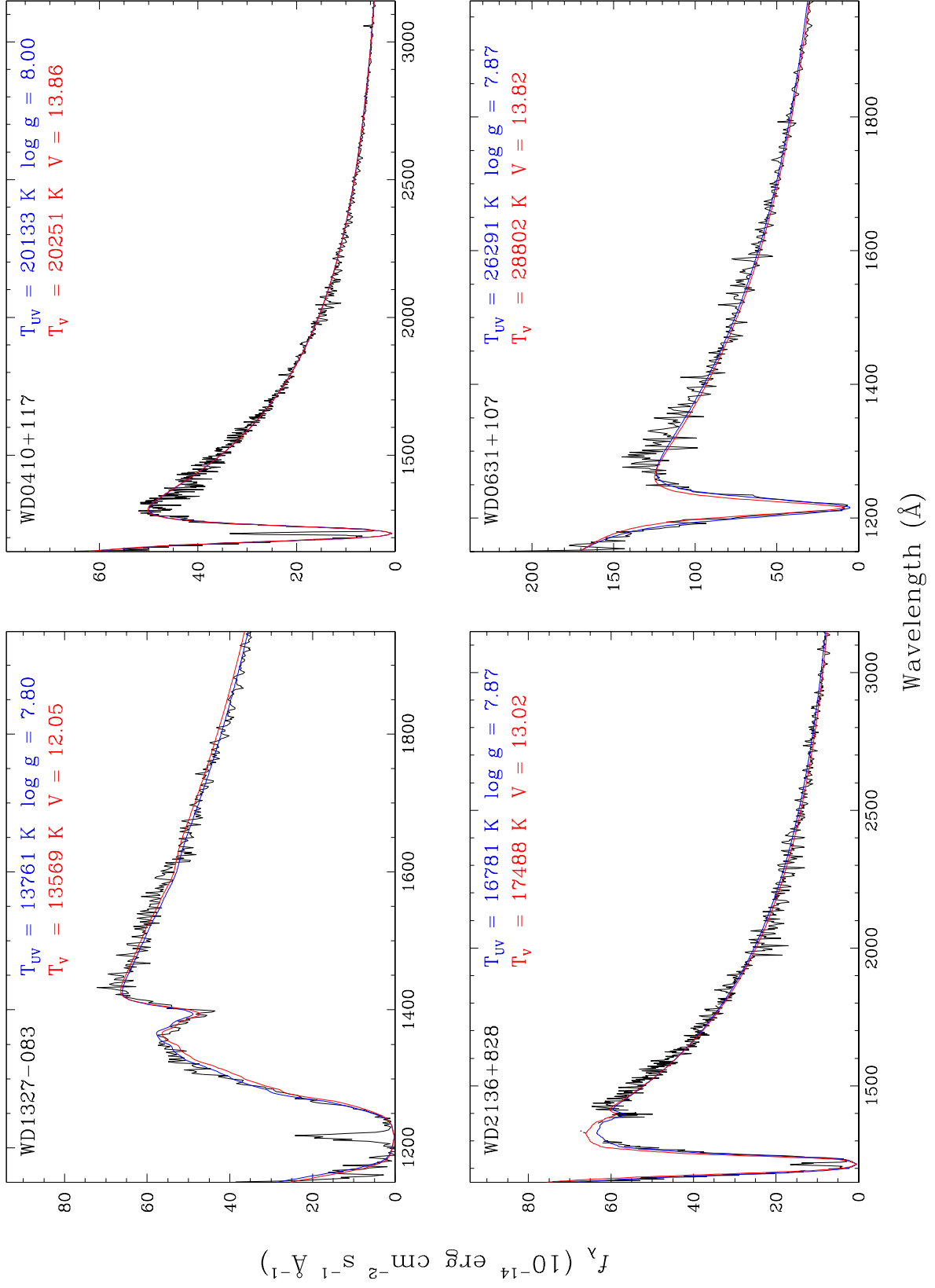


Figure 3

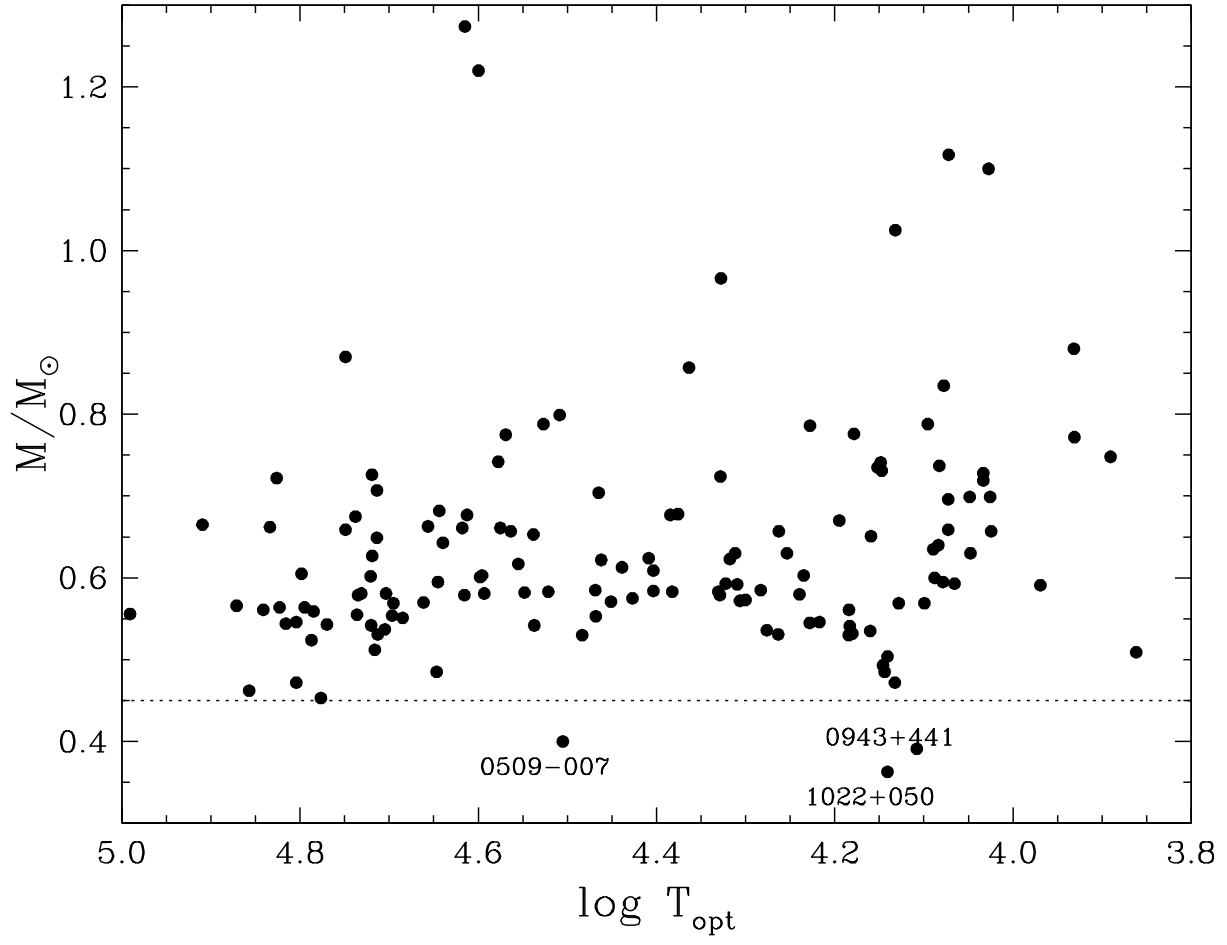


Figure 4

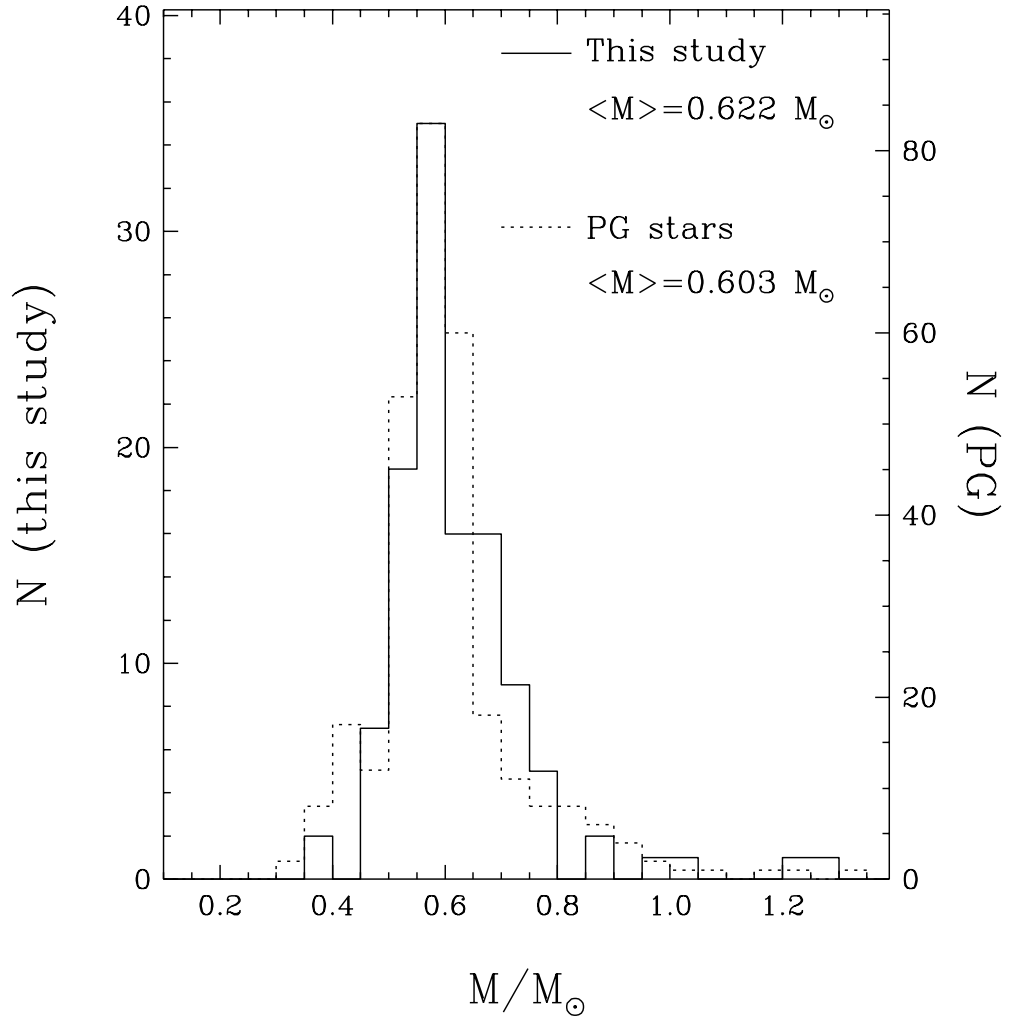


Figure 5

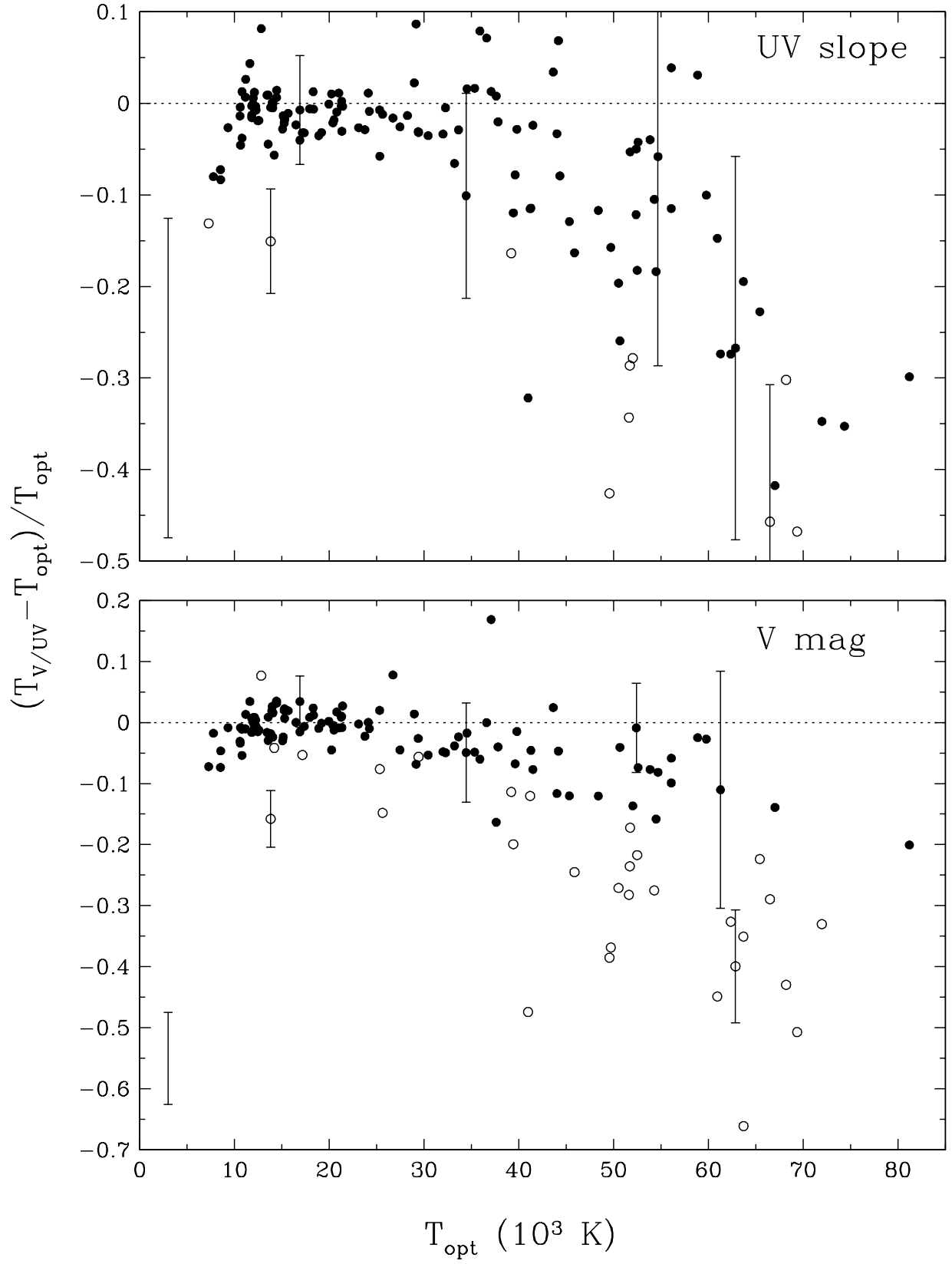


Figure 6

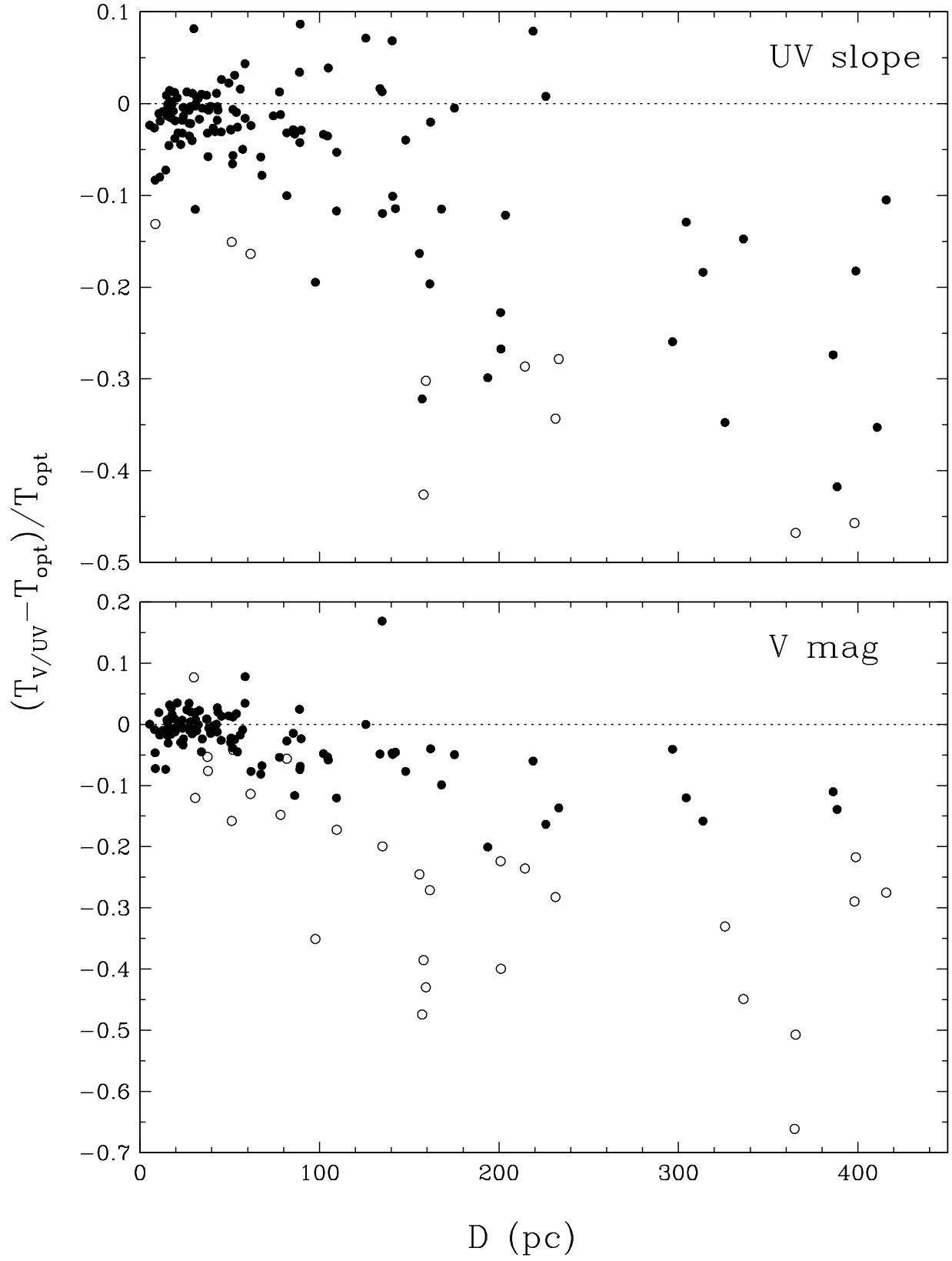


Figure 7

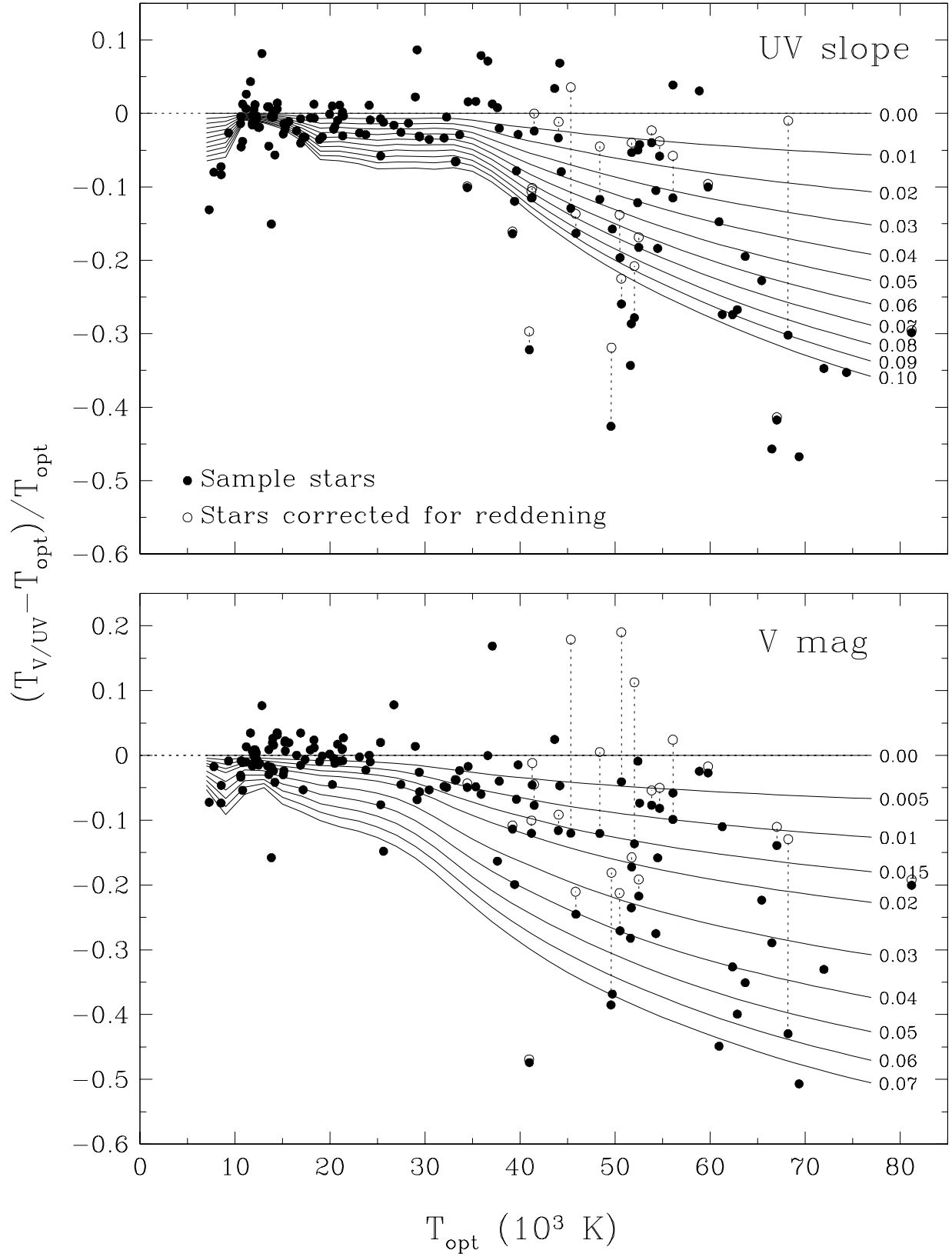


Figure 8

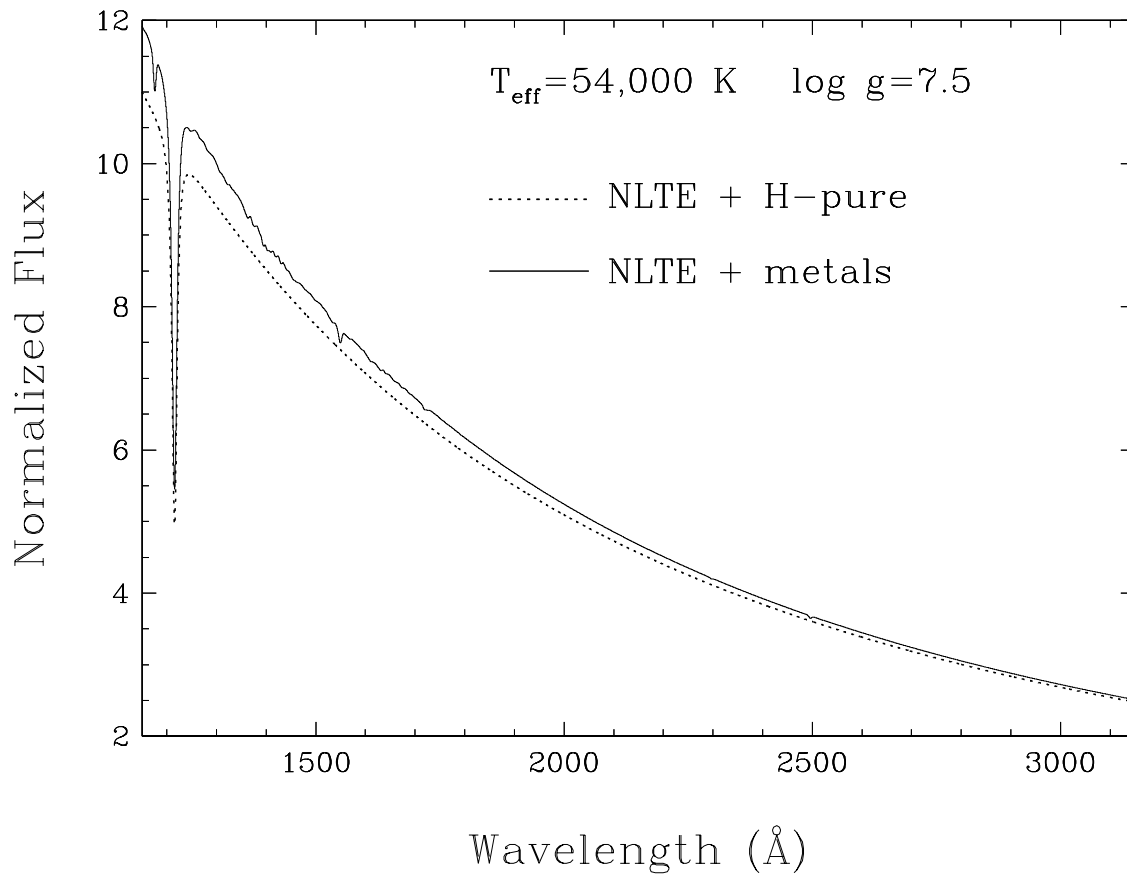


Figure 9

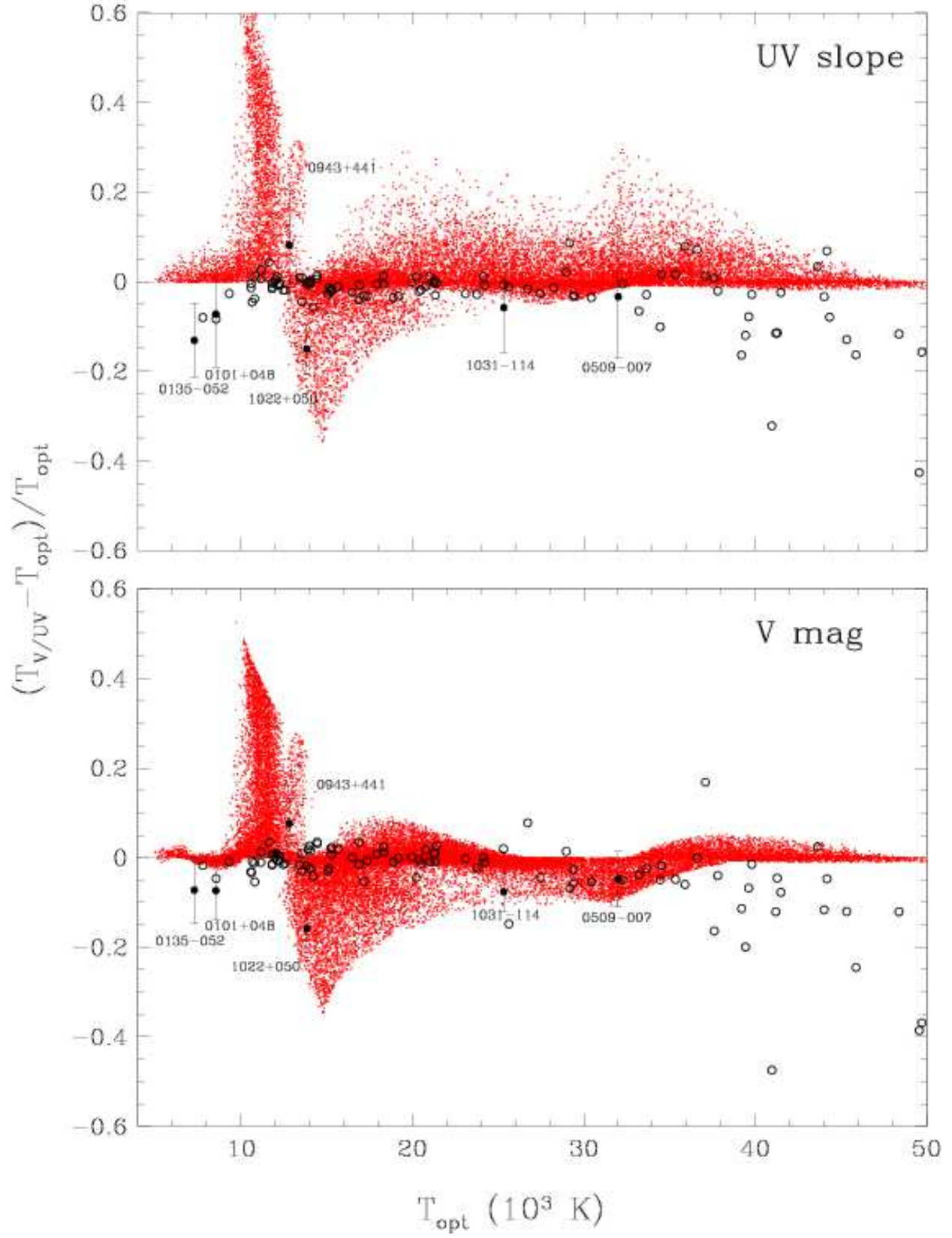


Figure 10

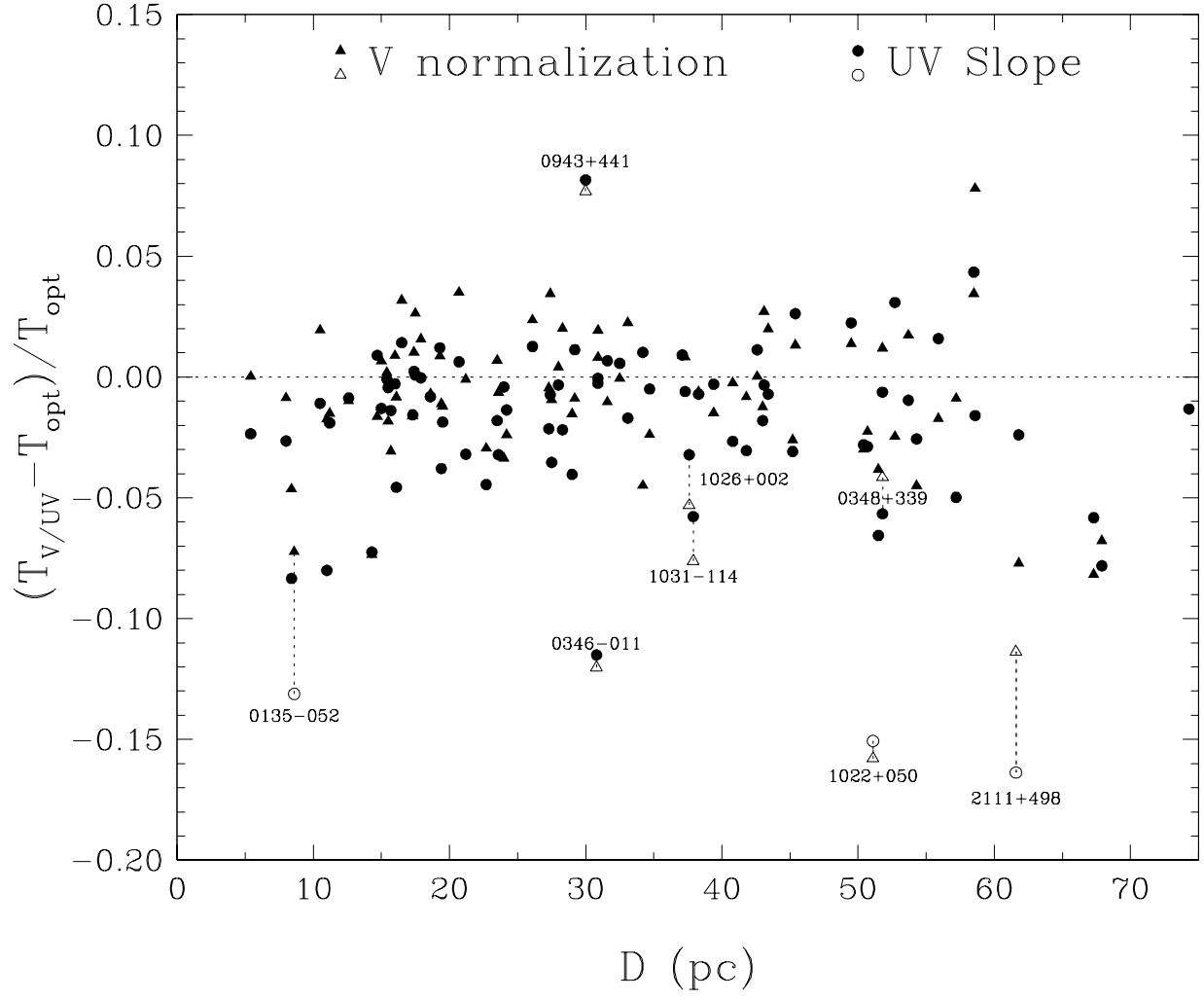


Figure 11